

NUMERICAL CALCULATION OF MODAL SPRING REVERB PARAMETERS

Maarten van Walstijn

Sonic Arts Research Centre
 School of Electronics, Electrical Engineering, and Computer Science
 Queen's University Belfast, UK
 m.vanwalstijn@qub.ac.uk

ABSTRACT

In the design of real-time spring reverberation algorithms, a modal architecture offers several advantages, including computational efficiency and parametric control flexibility. Due to the complex, highly dispersive behavior of helical springs, computing physically accurate parameters for such a model presents specific challenges. In this paper these are addressed by applying an implicit higher-order-in-space finite difference scheme to a two-variable model of helical spring dynamics. A novel numerical boundary treatment is presented, which utilises multiple centered boundary expressions of different stencil width. The resulting scheme is unconditionally stable, and as such allows adjusting the numerical parameters independently of each other and of the physical parameters. The dispersion relation of the scheme is shown to be accurate in the audio range only for very high orders of accuracy in combination with a small temporal and spatial step. The frequency, amplitude, and decay rate of the system modes are extracted from a diagonalised form of this numerical model. After removing all modes with frequencies outside the audio range and applying a modal amplitude correction to compensate for omitting the magnetic transducers, a light-weight modal reverb algorithm is obtained. Comparison with a measured impulse response shows a reasonably good match across a wide frequency range in terms of echo density, decay characteristics, and diffusive nature.

1. INTRODUCTION

Spring reverb tanks originated in the 1930s as a compact, electro-mechanic means to emulate room reverberation [1]. Their functionality relies on the slow and heavily dispersive propagation of waves in helical springs, which facilitates long reverberation times and diminishes constructive wave interference. The spring's vibrational behaviour is assumed to be approximately linear and time-invariant at typical driving levels, and the impulse response (IR) generally features a series of smeared pulses (see Figure 1). As discussed in previous works (see, e.g. [2, 3]), the IR spectrogram is typically divided into two frequency ranges, each featuring a series of frequency-dependent echos, sometimes referred to as chirps [4, 5]. These peculiar characteristics make spring reverb sonically distinct from room or plate reverb. As such, it has been appreciated and employed as an effect in its own right since the early 1960s, when type IV units first appeared [6].

Efforts have been made in the past two decades to digitally emulate spring reverb, which enables incorporating it into digi-

Copyright: © 2020 Maarten van Walstijn. This is an open-access article distributed under the terms of the Creative Commons Attribution 3.0 Unported License, which permits unrestricted use, distribution, and reproduction in any medium, provided the original author and source are credited.

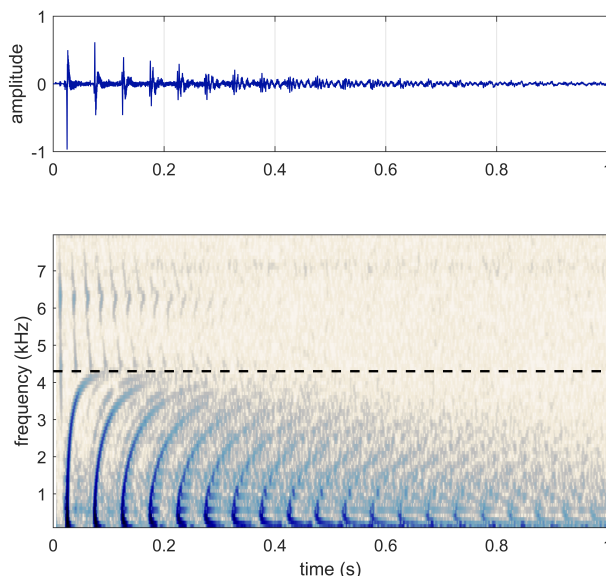


Figure 1: Example impulse response, measured on a single spring of an Accutronics & Belton 9EB2C1B Reverb tank. The black dashed line indicates the transition frequency.

tal music workflows. One approach aims to reproduce the chirps in a phenomenological manner, using allpass and lowpass filters within delay feedback structures [4, 5, 7]. Some of the response details, specifically those near and above the transition frequency, are difficult to capture this way, but otherwise good matches with measured IRs have been obtained, particularly so via automated calibration [8]. The main advantage is that the resulting computational structures are both efficient and parametric, i.e. the model parameters can be tuned on-line. The downside is that these parameters have no clear connection with the underlying physics of helical springs. One may therefore question the authenticity of the output if the parameters are significantly dialled away from those estimated directly from a measured IR.

Another phenomenological approach is to adopt a computational structure consisting of a parallel set of modal oscillators (see Figure 2) and set the modal frequencies according to physically-informed formulas [9, 10]. This also yields an efficient algorithm, and the modal architecture offers increased parametric control flexibility, as well a simple way of adding some diffusion in the IR tail [10]. However, physics-based approximate formulas have been proposed so far only for modes with frequencies below the transition frequency, and in addition it is unclear how similar closed-form expressions could be derived for mode amplitudes and damp-

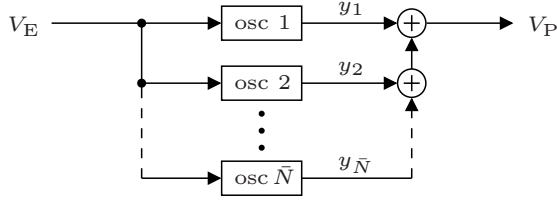


Figure 2: *Modal reverb architecture.* V_E and V_P are the excitation and pick-up voltage signals, respectively.

ing constants. In [10], this is addressed by setting these according to the amplitude envelope and overall decay rate of a measured IR.

The main alternative to the above methods is to model the vibrational behaviour of helical springs, and solve the resulting system of partial differential equations using numerical methods. Such an undiluted physical modelling approach intrinsically connects the model coefficients to the system’s material and geometrical parameters. Previous works have utilised second-order accuracy finite difference schemes for the discretisation of two-variable descriptions of helical spring dynamics [2, 11, 3, 12]. These models are based on different simplifying assumptions compared to the twelve-variable model by Wittrick [13]. So far, the magnetic beads at the spring terminations were incorporated only in the simpler model proposed in [11]. The otherwise more advanced “thin spring model” proposed in [3, 12] accounts for the dependency on the helix angle, and has been shown to behave extremely similar to Wittrick’s model in the audio range. The resulting numerical models capture much of the response detail, including secondary echos. On the other hand, numerical dispersion relation analysis results have indicated significant errors for high wavenumbers, even for parameterised schemes with optimally tuned coefficients. One of the more easily visible resulting artefacts is a discrepancy in the echo density above the transition frequency (see, e.g. Figure 6 in [11]). Compared with measured IRs the results computed in [2, 11] also lack diffusion in the IR tail [14]. In addition, all of the finite difference schemes proposed so far carry a relatively high computational load, making real-time implementation on standard processors less than straightforward.

This paper proposes a numerical method that aims to overcome both the accuracy and computational efficiency issues. Starting from a two-variable description of the helical spring dynamics in Section 2, the approach is to devise an unconditionally stable finite difference scheme in which the spatial derivatives are approximated with higher-order accuracy stencils (see Section 3). After selecting a sufficiently high sampling frequency, number of spatial segments and order of accuracy, the resulting scheme is diagonalised in Section 4 to obtain an efficient modal form which can be recast into a decimated version featuring only modes within the hearing range, and running at a standard audio rate.

2. SPRING REVERB TANK MODEL

2.1. Helical Spring Vibrations

In the below, the prime symbol is used to distinguish an original variable from a (non-primed) non-dimensional counterpart used throughout the main body of the paper. Consider a helical spring of cross-section $A = \pi r^2$, wire length L , helix radius R , Young’s

modulus, E , and mass density ρ . On basis of the simplifying assumptions made in [15], the transversal displacement $u' = u'(x', t)$ and longitudinal displacement $v' = v'(x', t)$ across the wire axis coordinate x' and time coordinate t can be considered to be governed by two coupled partial differential equations:

$$\frac{\partial^2 u'}{\partial t^2} = -\frac{r^2}{4\rho} \left(E + \eta \frac{\partial}{\partial t} \right) \left(\frac{\partial^4 u'}{\partial x'^4} + 2\epsilon^2 \frac{\partial^2 u'}{\partial x'^2} + \epsilon^4 u' \right) + \frac{\epsilon}{\rho} \left(E + \eta \frac{\partial}{\partial t} \right) \left(\frac{\partial v'}{\partial x'} - \epsilon u' \right) - 2\sigma \frac{\partial u'}{\partial t} + \frac{1}{\rho A} \mathcal{F}'_u, \quad (1)$$

$$\frac{\partial^2 v'}{\partial t^2} = \frac{1}{\rho} \left(E + \eta \frac{\partial}{\partial t} \right) \left(\frac{\partial^2 v'}{\partial x'^2} - \epsilon \frac{\partial u'}{\partial x'} \right) - 2\sigma \frac{\partial v'}{\partial t} + \frac{1}{\rho A} \mathcal{F}'_v, \quad (2)$$

where $\mathcal{F}'_u = \mathcal{F}'_u(x', t)$ and $\mathcal{F}'_v = \mathcal{F}'_v(x', t)$ are external force density terms, and $\epsilon = 1/R$. Frequency-dependent damping is incorporated here by considering the spring to behave like a Kelvin-Voigt material [16], in which η represents viscosity. Frequency-independent damping, which can loosely be considered to be due to the surrounding medium, is modelled through the damping parameter σ . Following the non-dimensionalisation proposed in [11], in which $x \in [0, 1]$, these equations can be re-written as

$$\frac{\partial^2 u}{\partial t^2} = -\kappa^2 \left(1 + \varphi \frac{\partial}{\partial t} \right) \left(\frac{\partial^4 u}{\partial x^4} + 2q^2 \frac{\partial^2 u}{\partial x^2} + q^4 u \right) + q^2 \gamma^2 \left(1 + \varphi \frac{\partial}{\partial t} \right) \left(\frac{\partial v}{\partial x} - u \right) - 2\sigma \frac{\partial u}{\partial t} + q \mathcal{F}_u, \quad (3)$$

$$\frac{\partial^2 v}{\partial t^2} = \gamma^2 \left(1 + \varphi \frac{\partial}{\partial t} \right) \left(\frac{\partial^2 v}{\partial x^2} - \frac{\partial u}{\partial x} \right) - 2\sigma \frac{\partial v}{\partial t} + \mathcal{F}_v, \quad (4)$$

where

$$u = \epsilon u', \quad v = \frac{v'}{L}, \quad x = \frac{x'}{L}, \quad \mathcal{F}_u = \frac{\mathcal{F}'_u}{\rho AL}, \quad \mathcal{F}_v = \frac{\mathcal{F}'_v}{\rho AL}. \quad (5)$$

$$\kappa = \sqrt{\frac{E}{\rho}} \frac{r}{2L^2}, \quad \gamma = \frac{1}{L} \sqrt{\frac{E}{\rho}}, \quad q = \epsilon L, \quad \varphi = \frac{\eta}{E}. \quad (6)$$

2.2. Boundary Conditions

A simplified form is considered here, omitting the magnets at either end of the system. This leaves various types of lossless boundary conditions to be considered, out of which the following is employed in this study:

$$v(0, t) = 0, \quad u(0, t) = 0 \quad \frac{\partial u}{\partial x}(0, t) = 0, \quad (7)$$

$$v(1, t) = 0, \quad u(1, t) = 0 \quad \frac{\partial u}{\partial x}(1, t) = 0. \quad (8)$$

From substitution into eq. (4) re-formulated with one-sided spatial second derivatives and assuming $\mathcal{F}_v(0, t) = \mathcal{F}_v(1, t) = 0$, one obtains

$$\frac{\partial^2 v}{\partial x^2}(0^+, t) = 0, \quad \frac{\partial^2 v}{\partial x^2}(1^-, t) = 0. \quad (9)$$

2.3. Input and Output

Given a voltage input signal $V_E(t)$, the driving terms in (3,4) are defined as

$$\mathcal{F}_u(x, t) = \xi \sin(\theta_E) \psi_E(x) V_E(t), \quad (10)$$

$$\mathcal{F}_v(x, t) = \xi \cos(\theta_E) \psi_E(x) V_E(t), \quad (11)$$

where θ_E is the ‘excitation angle’. For the purpose of modelling the reverb tank as an input-to-output system with reciprocal transducers, the relationship between the input/output voltage and the driving/pick-up force may be simplified to a simple scaling by an arbitrary constant ξ , which is set to $\xi = 1$ here. The term $\psi_E(x)$ is a distribution function of width w , positioned near the input end of the system. For example, a raised-cosine distribution:

$$\psi_E(x) = \begin{cases} \frac{1}{w} [1 + \cos(\pi x/w)] & : 0 < x < w \\ 0 & : \text{otherwise} \end{cases} \quad (12)$$

Using a reciprocal mechanism at the other end, the output voltage signal is defined as

$$\begin{aligned} V_P(t) = & -\frac{\sin(\theta_P)}{q\xi} \int_0^1 \psi_P(x) \left[-\kappa^2 \frac{\partial^4 u}{\partial x^4} - 2\kappa^2 q^2 \frac{\partial^2 u}{\partial x^2} \right. \\ & \left. - (\kappa^2 q^4 + q^2 \gamma^2) u(t) + q^2 \gamma^2 \frac{\partial v}{\partial x} \right] dx \\ & - \frac{\cos(\theta_P)}{\xi} \int_0^1 \psi_P(x) \gamma^2 \left[\frac{\partial^2 v}{\partial x^2} - \frac{\partial u}{\partial x} \right] dx, \end{aligned} \quad (13)$$

where $\psi_P(x) = \psi_E(1-x)$. The terms inside the square brackets are the force densities in the two polarisations. Hence the integrals calculate a weighted sum over force density. For $w \rightarrow 0$, each of the integrals reduces to the force exerted by the spring on the fixed end point.

The above clearly is a simplifying workaround that replaces a proper model for driving and sensing through the magnets at each end, such as that proposed in [11]. The motivation behind this choice is to keep the boundary model as simple as possible in this initial attempt to apply higher-order spatial schemes. Note though that the main ramifications can be compensated for in a phenomenological fashion within the final modal form (see Section 4.3).

2.4. Dispersion Relation

Considering a single frequency (ω) and ignoring damping and driving forces, waves travelling through the spring may be written in terms of frequency and accompanying (dimensionless) wave number (β) as

$$u(x, t) = U e^{j(\omega t + \beta x)}, \quad v(x, t) = V e^{j(\omega t + \beta x)}, \quad (14)$$

where U and V are complex amplitudes, and $j = \sqrt{-1}$. Substituting (14) into (3,4) omitting the driving terms yields the following system of equations [11]:

$$\begin{bmatrix} \omega^2 - \kappa^2(\beta^2 - q^2)^2 - q^2 \gamma^2 & jq^2 \gamma^2 \beta \\ -j\gamma^2 \beta & \omega^2 - \gamma^2 \beta^2 \end{bmatrix} \begin{bmatrix} U \\ V \end{bmatrix} = \begin{bmatrix} 0 \\ 0 \end{bmatrix}. \quad (15)$$

The nontrivial solutions occur when the determinant equals zero:

$$\omega^4 - \underbrace{[\kappa^2(\beta^2 - q^2)^2 + \gamma^2(\beta^2 + q^2)]}_B \omega^2 + \underbrace{\gamma^2 \beta^2 \kappa^2(\beta^2 - q^2)^2}_C = 0. \quad (16)$$

This has positive solutions for ω

$$\omega = \sqrt{\frac{B \pm \sqrt{B^2 - 4C}}{2}}. \quad (17)$$

In other words, we can relate any specific wave number to two frequencies, one of which systematically falls outside the hearing range [11]. Therefore only the low-frequency dispersion relation is considered here.

3. FINITE-DIFFERENCE SCHEME

3.1. Discretisation

Using a temporal step $\Delta_t = 1/f_s$ and spatial step $\Delta_x = 1/M$, the system variables are modelled at discrete points in space and time using the indexed with n and m , respectively:

$$u_m^n := u(m\Delta_x, n\Delta_t), \quad v_m^n := v(m\Delta_x, n\Delta_t), \quad (18)$$

where n and m are For the purpose of approximation of time derivatives, we define the difference and average operators

$$\delta u_m^n = u_m^{n+\frac{1}{2}} - u_m^{n-\frac{1}{2}}, \quad (19)$$

$$\mu u_m^n = \frac{1}{2} \left(u_m^{n+\frac{1}{2}} + u_m^{n-\frac{1}{2}} \right), \quad (20)$$

which can be combined in various ways to construct second-order accuracy centered difference and averaging operators:

$$\delta_1 u_m^n = \delta \mu u_m^n = \frac{1}{2} (u_m^{n+1} - u_m^{n-1}) \approx \Delta_t \frac{\partial u}{\partial t}(m\Delta_x, n\Delta_t), \quad (21)$$

$$\delta_2 u_m^n = \delta \delta u_m^n = u_m^{n+1} - 2u_m^n + u_m^{n-1} \approx \Delta_t^2 \frac{\partial^2 u}{\partial t^2}(m\Delta_x, n\Delta_t), \quad (22)$$

$$\mu_2 u_m^n = \mu \mu u_m^n = \frac{1}{4} (u_m^{n+1} + 2u_m^n + u_m^{n-1}) \approx u(m\Delta_x, n\Delta_t). \quad (23)$$

For approximation of spatial derivatives, higher-order accuracy centered difference operators are employed, which are denoted here as

$$\mathcal{D}_p u_m^n = \sum_{k=-K_p}^{K_p} d_{p,k} u_{m+k}^n \approx \Delta_x^p \frac{\partial^p u}{\partial x^p}(m\Delta_x, n\Delta_t), \quad (24)$$

for approximation of the p th derivative with a stencil of width $(2K_p + 1)$. For the three featuring spatial operators (\mathcal{D}_1 , \mathcal{D}_2 , \mathcal{D}_4) to be of the same order of accuracy, we have to choose

$$K_1 = K - 1, \quad K_2 = K - 1, \quad K_4 = K, \quad (25)$$

where K sets an overall scheme stencil width of $(2K + 1)$ and order of accuracy of $(2K - 2)$. In practice we set the stencil of \mathcal{D}_1 and \mathcal{D}_2 to the same width as that of \mathcal{D}_4 , by adding a zero weight on either side. The smallest possible scheme width parameter is $K = 2$, which yields second-order accurate approximations of the spatial derivatives. The coefficients $d_{p,k}$ are calculated using the usual recursive formulation [17]. The operator in (24) is used for all nodes within the spatial domain of the system, including those immediately adjacent to the system boundaries. This means that, for both polarisations, $(K - 1)$ so-called *ghost nodes* have to be considered on either end of the system (see Figure 3).

Finally, the calculation of the discrete-domain counterpart of a specific distribution function $\psi_\phi(x)$ is not performed by straight sampling, but instead using the integral

$$\bar{\psi}_{\phi,m} = \frac{1}{\Delta_x} \int_0^1 \nu_m(x) \psi_\phi(x) dx, \quad (\phi = E, P) \quad (26)$$

where $\nu_m(x)$ is a triangular nodal catchment function:

$$\nu_m(x) = \begin{cases} x/\Delta_x + (1-m) & : (m-1)\Delta_x \leq x < m\Delta_x \\ -x/\Delta_x + (1+m) & : m\Delta_x \leq x \leq (m+1)\Delta_x \\ 0 & : \text{otherwise} \end{cases} \quad (27)$$

For the case of a point distribution (i.e. $\psi_\phi(x)$ is a Dirac delta function), the use of (26) amounts to linear (de-)interpolation.

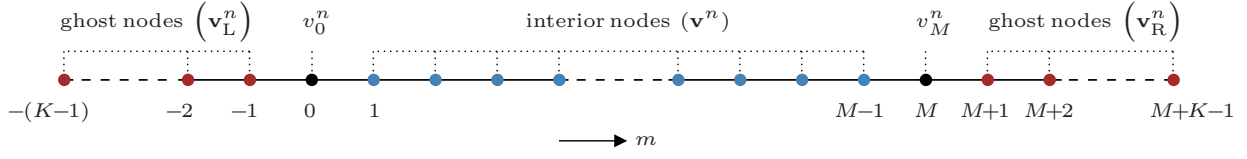


Figure 3: Spatial grid for a finite difference model that divides the domain length into M segments, resulting into $(M - 1)$ interior domain nodes, and employing a spatial stencil of width $(2K + 1)$. The blue nodes indicate the interior domain points, and the red nodes represent ghost-nodes. The two boundary points, which are zero-valued for the chosen boundary conditions, are indicated with black.

3.1.1. Helical Spring

Employing the operators defined in (22,23,24), equations (3,4) are discretised as follows:

$$\delta_2 u_m^n = (\mu_2 + \zeta \delta_1) \left[(-g_4 \mathcal{D}_4 - g_2 \mathcal{D}_2 - g_0) u_m^n + g_1 \mathcal{D}_1 v_m^n \right],$$

$$- \chi \delta_1 u_m^n + q \mathcal{F}_u^n \Delta_t^2, \quad (28)$$

$$\delta_2 v_m^n = (\mu_2 + \zeta \delta_1) \left[h_2 \mathcal{D}_2 v_m^n - h_1 \mathcal{D}_1 u_m^n \right]$$

$$- \chi \delta_1 v_m^n + \mathcal{F}_v^n \Delta_t^2, \quad (29)$$

where

$$g_0 = (\kappa^2 q^4 + q^2 \gamma^2) \Delta_t^2, \quad g_1 = \frac{q^2 \gamma^2 \Delta_t^2}{\Delta_x}, \quad g_2 = \frac{2\kappa^2 q^2 \Delta_t^2}{\Delta_x^2}, \quad (30)$$

$$g_4 = \frac{\kappa^2 \Delta_t^2}{\Delta_x^4}, \quad \zeta = \frac{\varphi}{2\Delta_t}, \quad \chi = 2\sigma \Delta_t, \quad h_1 = \frac{\gamma^2 \Delta_t^2}{\Delta_x}, \quad h_2 = \frac{\gamma^2 \Delta_t^2}{\Delta_x^2}. \quad (31)$$

The averaging operator μ_2 is employed on all restoring forces for the purpose of constructing an unconditionally stable scheme (see the Appendix).

3.1.2. Boundary Conditions

From the first two conditions in (7) and (8), we can simply set

$$u_0^n = 0, \quad v_0^n = 0, \quad u_M^n = 0, \quad v_M^n = 0. \quad (32)$$

For the third condition in both (7) and (8), as well as the accompanying results in (9), we apply centered difference operators in repeated form, using a larger spatial step each time. This can be specified as

$$u_k^n = u_{-k}^n, \quad v_k^n = -v_{-k}^n, \quad (33)$$

$$u_{M+k}^n = u_{M-k}^n, \quad v_{M+k}^n = -v_{M-k}^n \quad (34)$$

where $k = 1, 2, \dots, (K - 1)$. Given the symmetries $d_{1,k} = -d_{1,-k}$ and $d_{2,k} = d_{2,-k}$, this means that numerical versions of the boundary conditions with the orders of accuracy ranging from 2 to $2K - 2$ are all simultaneously satisfied. For example, at the left-hand termination we have

$$\mathcal{D}_2^{(\Upsilon)} u_0^n = \sum_{k=1}^{\Upsilon} d_{2,k} (u_k^n - u_{-k}^n) = 0, \quad (\Upsilon = 1, 2, \dots, K - 1), \quad (35)$$

$$\mathcal{D}_1^{(\Upsilon)} v_0^n = \sum_{k=1}^{\Upsilon} d_{1,k} (v_k^n + v_{-k}^n) = 0, \quad (\Upsilon = 1, 2, \dots, K - 1), \quad (36)$$

where $\mathcal{D}_p^{(\Upsilon)}$ temporarily denotes the spatial differetiator for stencil width Υ . Equations (33,34) will be used to eliminate the total of $4(K - 1)$ ghost nodes.

3.1.3. Input and Output

Using the discrete weights defined in (26), equations (10,11) become

$$\mathcal{F}_{u,m}^n = \xi \sin(\theta_E) \bar{\psi}_{E,m} V_E^n, \quad (37)$$

$$\mathcal{F}_{v,m}^n = \xi \cos(\theta_E) \bar{\psi}_{E,m} V_E^n, \quad (38)$$

and the discrete-domain output signal is:

$$V_P^n = \left\{ \frac{\sin(\theta_P)}{q\xi} \sum_{m=1}^{M-1} \bar{\psi}_{P,m} \left[(g_4 \mathcal{D}_4 + g_2 \mathcal{D}_2 + g_0) u_m^n - g_1 \mathcal{D}_1 v_m^n \right] \right.$$

$$\left. + \frac{\cos(\theta_P)}{\xi} \sum_{m=1}^{M-1} \bar{\psi}_{P,m} \left[h_1 \mathcal{D}_1 u_m^n - h_2 \mathcal{D}_2 v_m^n + \right] \right\} \Delta_x. \quad (39)$$

3.2. Vector-Matrix Formulation

Let's define \mathbf{v}^n and \mathbf{u}^n as column vectors holding the $(M - 1)$ interior node values of the longitudinal and transversal dimension. Applying (24) across all of the interior nodes on the v -axis, we can then write

$$\mathcal{D}_p \mathbf{v}^n = \tilde{\mathbf{D}}_p \tilde{\mathbf{v}}^n, \quad (40)$$

where $\tilde{\mathbf{v}}^n$ is a column vector of length $M + 2K - 3$ holding all the node values required for the calculation:

$$\tilde{\mathbf{v}}^n = \left[(\mathbf{v}_L^n)^T \quad 0 \quad (\mathbf{v}^n)^T \quad 0 \quad (\mathbf{v}_R^n)^T \right]^T, \quad (41)$$

and $\tilde{\mathbf{D}}$ is a $(M + 2K - 3) \times (M - 1)$ matrix with elements

$$\tilde{D}_{p,i,j} = d_{p,i-j-K+1}. \quad (42)$$

Figure 4 schematically depicts the form of this matrix, and the vectors in (41) are defined as shown in Figure 3. Using the matrix partitioning defined in Figure 4, equation (40) can be written

$$\mathcal{D}_p \mathbf{v}^n = \tilde{\mathbf{A}}_p \mathbf{v}_L^n + \tilde{\mathbf{B}}_p \mathbf{v}^n + \tilde{\mathbf{C}}_p \mathbf{v}_R^n. \quad (43)$$

Similarly for u , we can write

$$\mathcal{D}_p \mathbf{u}^n = \tilde{\mathbf{A}}_p \mathbf{u}_L^n + \tilde{\mathbf{B}}_p \mathbf{u}^n + \tilde{\mathbf{C}}_p \mathbf{u}_R^n. \quad (44)$$

From the repeated boundary conditions in (33,34), we can write

$$\tilde{\mathbf{A}}_p \mathbf{v}_L^n = \left[-\tilde{\mathbf{A}}_p' \quad \tilde{\mathbf{0}} \right] \mathbf{v}^n, \quad \tilde{\mathbf{C}}_p \mathbf{v}_R^n = \left[\tilde{\mathbf{0}} \quad -\tilde{\mathbf{C}}_p' \right] \mathbf{v}^n, \quad (45)$$

$$\tilde{\mathbf{A}}_p \mathbf{u}_L^n = \left[\tilde{\mathbf{A}}_p' \quad \tilde{\mathbf{0}} \right] \mathbf{u}^n, \quad \tilde{\mathbf{C}}_p \mathbf{u}_R^n = \left[\tilde{\mathbf{0}} \quad \tilde{\mathbf{C}}_p' \right] \mathbf{u}^n, \quad (46)$$

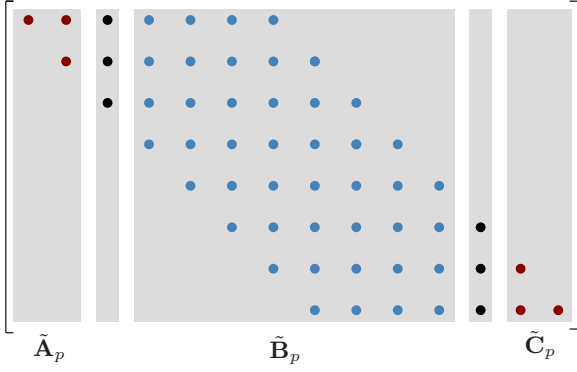


Figure 4: Example of the form of the matrix $\tilde{\mathbf{D}}_p$ for $M = 9$ and $K = 3$. The dots indicate non-zero matrix entries. The red dots indicate finite difference weights applying to ghost-nodes.

where the apostrophe indicates the left-right flipping of a matrix, and $\tilde{\mathbf{0}}$ is a zero matrix of size $(M - K) \times (M - 1)$. Substitution into (43) and (44) yields

$$\mathcal{D}_p \mathbf{v}^n = \mathbf{D}_p^v \mathbf{v}^n, \quad \mathcal{D}_p \mathbf{u}^n = \mathbf{D}_p^u \mathbf{u}^n, \quad (47)$$

where

$$\mathbf{D}_p^u = \begin{bmatrix} \tilde{\mathbf{A}}_p' & \tilde{\mathbf{0}} \end{bmatrix} + \tilde{\mathbf{B}}_p + \begin{bmatrix} \tilde{\mathbf{0}} & \tilde{\mathbf{C}}_p' \end{bmatrix}, \quad (48)$$

$$\mathbf{D}_p^v = \begin{bmatrix} -\tilde{\mathbf{A}}_p' & \tilde{\mathbf{0}} \end{bmatrix} + \tilde{\mathbf{B}}_p + \begin{bmatrix} \tilde{\mathbf{0}} & -\tilde{\mathbf{C}}_p' \end{bmatrix}, \quad (49)$$

We may now write (28,29) in vector-matrix form:

$$\delta_2 \mathbf{u}^n = (\mu_2 + \zeta \delta_1) \left[-(g_4 \mathbf{D}_4^u + g_2 \mathbf{D}_2^u + g_0 \mathbf{I}) \mathbf{u}^n + g_1 \mathbf{D}_1^v \mathbf{v}^n \right] - \chi \delta_1 \mathbf{u}^n + q \mathcal{F}_u^n \Delta_t^2, \quad (50)$$

$$\delta_2 \mathbf{v}^n = (\mu_2 + \zeta \delta_1) \left[-h_1 \mathbf{D}_1^u \mathbf{u}^n + h_2 \mathbf{D}_2^v \mathbf{v}^n \right] - \chi \delta_1 \mathbf{v}^n + \mathcal{F}_v^n \Delta_t^2. \quad (51)$$

Combining the two equations and substituting (37,38), the whole system can be written in terms of vectors of length $N = 2(M - 1)$:

$$\delta_2 \mathbf{w}^n = \left[(\mu_2 + \zeta \delta_1) \mathbf{D} - \chi \delta_1 \mathbf{I} \right] \mathbf{w}^n + \mathbf{g}_E V_E^n \Delta_t^2, \quad (52)$$

where

$$\mathbf{w}^n = \begin{bmatrix} \mathbf{u}^n \\ \mathbf{v}^n \end{bmatrix}, \quad \mathbf{g}_E = \begin{bmatrix} q \xi \sin(\theta_E) \bar{\Psi}_E \\ \xi \cos(\theta_E) \bar{\Psi}_E \end{bmatrix}, \quad (53)$$

$$\mathbf{D} = \begin{bmatrix} -(g_4 \mathbf{D}_4^u + g_2 \mathbf{D}_2^u + g_0 \mathbf{I}^u) & g_1 \mathbf{D}_1^v \\ -h_1 \mathbf{D}_1^u & h_2 \mathbf{D}_2^v \end{bmatrix}, \quad (54)$$

and where \mathbf{I}^u and \mathbf{I} are identity matrices of size $(M - 1) \times (M - 1)$ and $N \times N$, respectively, and $\bar{\Psi}_E$ is a column vector holding values as defined by (26) with $\phi = E$. The output can be computed as

$$V_P^n = \mathbf{g}_P \mathbf{D} \mathbf{w}^n, \quad (55)$$

where

$$\mathbf{g}_P = -\Delta_x \left[(q \xi)^{-1} \sin(\theta_P) \bar{\Psi}_P \quad \xi^{-1} \cos(\theta_P) \bar{\Psi}_P \right], \quad (56)$$

with the elements of the column vector $\bar{\Psi}_P$ defined by (26).

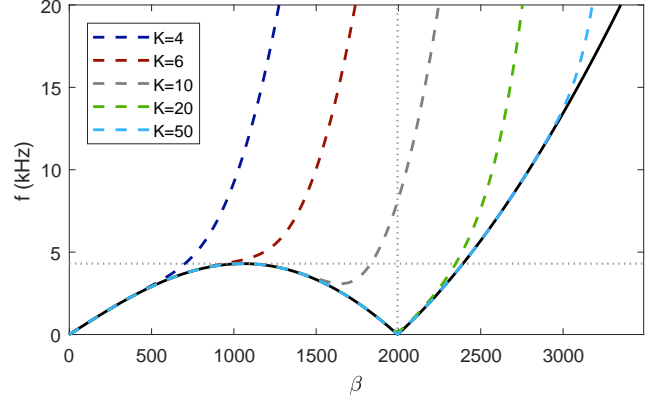


Figure 5: Dispersion relations. The solid black line is the continuous-domain curve. The horizontal dotted line indicates the spring's transition frequency, and the vertical dotted line marks $\beta = q$. All curves were evaluated using the spring parameters listed in the first column of Table 1, but with $\phi = \sigma = 0$. The numerical dispersion relations were evaluated with $f_s = 1$ MHz and $M = 1300$. For any value of K , the associated stencil width is $(2K + 1)$ and the scheme order of accuracy is $(2K - 2)$.

3.3. Dispersion Analysis

Analogous to (14), we can explore the ansatz

$$u_m^n = U e^{j(\omega n \Delta_t + \beta m \Delta_x)}, \quad v_m^n = V e^{j(\omega n \Delta_t + \beta m \Delta_x)}. \quad (57)$$

After substitution into (50,51), one obtains

$$\begin{bmatrix} \tau + (g_4 \mathcal{D}_4 + g_2 \mathcal{D}_2 + g_0) & -g_1 \mathcal{D}_1 \\ h_1 \mathcal{D}_1 & \tau - h_2 \mathcal{D}_2 \end{bmatrix} \begin{bmatrix} U \\ V \end{bmatrix} = \begin{bmatrix} 0 \\ 0 \end{bmatrix}. \quad (58)$$

where

$$\tau = -4 \tan^2\left(\frac{1}{2} \omega \Delta_t\right), \quad (59)$$

$$\mathcal{D}_p = \sum_{k=-K}^K d_{p,k} e^{j k \beta \Delta_x}. \quad (60)$$

The term τ can be solved for from (58), after which frequency ω is extracted using (59).

Figure 5 displays the numerical dispersion relation for different values of K , with the continuous-domain curve also shown for comparison. A 1 MHz sampling frequency was chosen so that errors due to time derivative approximations are negligible for frequencies below 20 kHz, and the number of segments was set to $M = 1300$ to ensure that the system possesses a sufficient number of modes within the audio range. Setting $\theta_E = \theta_P = 90^\circ$, which corresponds to exciting only the transversal polarisation, is motivated by (a) the experimental observation by Parker [18] that the electromagnetic field drives the magnets mainly into rotational motion, which does not directly couple to the longitudinal spring vibration polarisation, and (b) the empirical observation by the current author that the numerical model's impulse response then most closely resembles the measured response.

Table 1: System parameter values.

spring parameters			magnet-related parameters		
κ	0.02018	[s ⁻¹]	f_{co}	100	[Hz]
q	1994		p	1.8	
γ	1200	[s ⁻¹]	f_c	6300	[Hz]
ϕ	2.0×10^{-8}	[s]	f_b	300	[Hz]
σ	3.0	[s ⁻¹]	H_c	16	
w	0.004	[m]	R_0	1.2	
θ_E	90	[degrees]	f_D	600	[Hz]
θ_P	90	[degrees]	v	3	

4. MODAL REVERBERATOR

4.1. Diagonalisation

In order to transform the scheme in (52) to a set of uncoupled update equations, the matrix \mathbf{D} is diagonalised:

$$\mathbf{D} = \mathbf{P}\mathbf{Q}\mathbf{P}^{-1}, \quad (61)$$

where \mathbf{Q} is a diagonal matrix holding the eigenvalues of \mathbf{D} and \mathbf{P} is a full and invertible matrix holding the eigenvectors of \mathbf{D} . Substitution into (52) and pre-multiplying with \mathbf{P}^{-1} then gives

$$\delta_2 \mathbf{y}^n = \left[(\mu_2 + \zeta \delta_1) \mathbf{Q} - \chi \delta_1 \mathbf{I} \right] \mathbf{y}^n + \mathbf{P}^{-1} \mathbf{g}_E V_E^n \Delta_t^2, \quad (62)$$

where $\mathbf{y}^n = \mathbf{P}^{-1} \mathbf{w}^n$ is a new coordinate vector. After applying the operators, this can be algebraically re-worked into the update equation

$$\mathbf{y}^{n+1} = \mathbf{A}\mathbf{y}^n + \mathbf{B}\mathbf{y}^{n-1} + \mathbf{c}_E V_E^n \Delta_t^2, \quad (63)$$

where

$$\mathbf{A} = \mathbf{S}^{-1} [2\mathbf{I} + \frac{1}{2}\mathbf{Q}], \quad (64)$$

$$\mathbf{B} = \mathbf{S}^{-1} [(\frac{1}{2}\chi - 1)\mathbf{I} + (\frac{1}{4} - \frac{1}{2}\zeta)\mathbf{Q}], \quad (65)$$

$$\mathbf{c}_E = \mathbf{S}^{-1} \mathbf{P}^{-1} \mathbf{g}_E, \quad (66)$$

$$\mathbf{S} = (\frac{1}{2}\chi + 1)\mathbf{I} - (\frac{1}{4} + \frac{1}{2}\zeta)\mathbf{Q}. \quad (67)$$

Given that \mathbf{Q} is diagonal, so are \mathbf{A} and \mathbf{B} , meaning that (63) is set of uncoupled second-order difference equations, each representing the dynamics of a single mode of the system. The output can be obtained from the modal displacements \mathbf{y}^n as $V_P^n = \mathbf{g}_P \mathbf{w}^n = \mathbf{c}_P \mathbf{y}^n$, where $\mathbf{c}_P = \mathbf{g}_P \mathbf{Q}\mathbf{P}$.

4.2. Modal Reverb Algorithm

Using the ansatz $y^n = e^{sn\Delta_t} = e^{(j\omega - \alpha)n\Delta_t}$, the relationship between the diagonal elements of \mathbf{A} and \mathbf{B} and the mode frequencies and decay rates can be derived:

$$A_{i,i} = 2e^{-\alpha_i \Delta_t} \cos(\omega_i \Delta_t), \quad B_{i,i} = -e^{-2\alpha_i \Delta_t}, \quad (68)$$

which is known in digital filter theory as the impulse invariant method [19]. Using (68) we can extract the N system mode frequencies and decay rates; the associated modal shapes are represented (in spatially sampled form) by the N matching eigenvectors contained as a column vectors in \mathbf{P} . Many of the modes obtained this way when using a 1 MHz sampling frequency will lie outside the hearing range. Therefore, new modal update equations

are constructed using a standard audio rate $\bar{f}_s = 1/\bar{\Delta}_t^2$, taking the form

$$\mathbf{y}_j^{n+1} = a_j \mathbf{y}_j^n + b_j \mathbf{y}_j^{n-1} + c_j V_E^n \bar{\Delta}_t^2, \quad (69)$$

where a_j and b_j are defined through (68) using $\bar{\Delta}_t$ instead of Δ_t , and where $j = i$ only when $f_i < 20 \text{ kHz} < \frac{1}{2} \bar{f}_s$. Consolidating the modal input and output weights, the modal amplitudes are $c_j = c_{E,j} \cdot c_{P,j}$. Accordingly, the output can be computed simply as the sum of the modal oscillator outputs, thus arriving at the modal reverb architecture shown in Figure 2. For the system values listed in Table 1, the finite difference model possesses a total of 2598 modes. This is reduced to 1009 modes in the final modal structure, which can be easily implemented in real-time on standard processors (see, e.g. [20]).

Figure 6 shows an example of the distribution of mode amplitudes c_j and mode decay rates α_j against mode frequencies up to 6 kHz. Noticeable is the increase in modal density near the transition frequency, and the quasi-harmonic series at the higher frequencies. As seen in the lower plot, the decay rate is a monotonically rising function of mode frequency, matching σ at frequencies near zero.

4.3. Modal Manipulations

From the upper plot in Figure 6 it can be seen that the numerical model impulse response will be high-pass. In a reverb tank, the magnets at the input and output end introduce various resonances, the main one lying at a very low frequency, as such creating a low-pass effect. A second resonance often appears at a frequency above the transition frequency [3]. For the purpose of visual and aural comparison with a measured impulse response, the resonance effects due to the magnets is modelled in a phenomenological manner here by filtering directly in the modal domain:

$$c'_j = H_{lp}(f_j) \cdot H_{pk}(f_j) \cdot c_j, \quad (70)$$

where

$$H_{lp}(f) = \frac{f_{co}^p}{f_{co}^p + f^p}, \quad (71)$$

$$H_{pk}(f) = 1 + (H_c - 1) \frac{f_b^2}{f_b^2 + (f - f_c)^2}, \quad (72)$$

can be considered as zero-phase filter responses of ‘low-pass’ and ‘peak filter’ type, respectively. The cut-off frequency f_{co} and roll-off steepness parameter p as well as the center frequency f_c , bandwidth f_b , and peak gain H_c can easily be determined through comparison with a measured impulse response. The magnets also cause a form of dispersion (decrease in echo density) at low frequencies, because waves at or near the main resonance mentioned above bring the magnets into motion more easily than high frequencies, thus experiencing a larger phase shift. This can be modelled in the modal domain by adjusting the mode frequencies as follows:

$$f'_j = \frac{1}{R(f_j)} \cdot f_j, \quad (73)$$

where $R(f)$ represents the ratio by which the inter-pulse time interval is increased

$$R(f) = 1 + (R_0 - 1) \left(\frac{f_D}{f + f_D} \right)^v. \quad (74)$$

The parameter R_0 is the maximum ratio (occurring at zero-frequency), and f_D is the frequency below which the low-frequency dispersion takes effect. The exponent v controls the sharpness of the ‘bend’ in the echo density pattern.

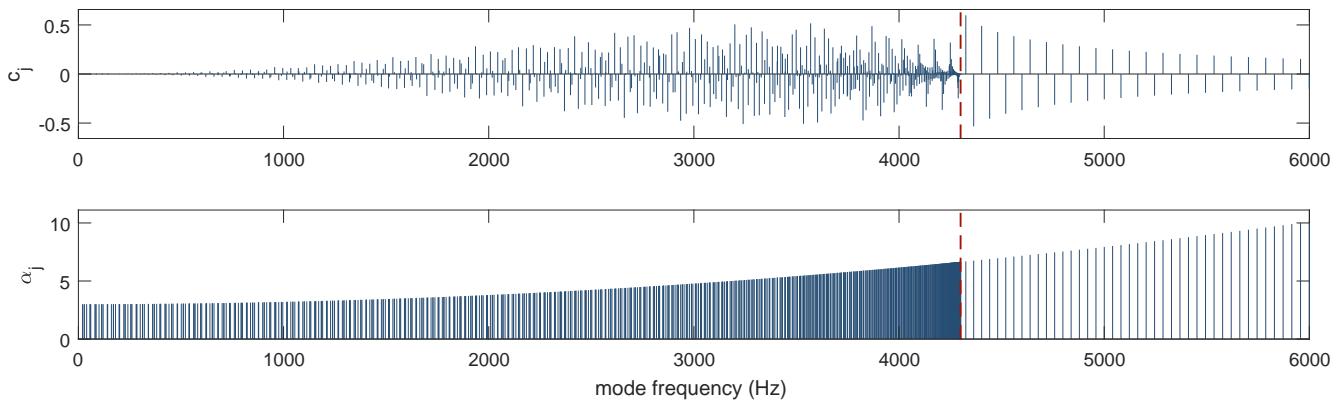


Figure 6: Mode amplitude (c_j) and decay rate (α_j) plotted against mode frequency (f_j), for the spring parameters listed in the first column of Table 1. The red dashed line indicates the spring's transition frequency. The numerical parameters used are $f_s = 1$ MHz, $M = 1300$, and $K = 50$.

4.4. Comparison with a Measured Impulse Response

The impulse response of the numerical modal was calculated using the numerical parameters $f_s = 1$ MHz, $M = 1300$, and $K = 50$; the modal synthesis was performed using $\tilde{f}_s = 44.1$ kHz. The upper plot in Figure 7 re-displays the spectrogram of the IR measured on an Accutronics & Belton 9EB2C1B Reverb tank shown earlier in Figure 1, and the lower plot shows the computed IR. The parameters κ and q (listed in Table 1) were tuned to match the transition frequency and low-frequency echo density of the measured response. It can be seen that this results in an excellent match in echo density at frequencies below as well as above the transition frequency. Also visible from the comparison is that the simulated response exhibits an appropriate level of temporal blurring at frequencies between 1 and 4 kHz, and that the overall frequency-dependent energy decay pattern is modelled reasonably well with the two chosen damping parameters. Both impulse responses are available for aural comparison on the companion webpage¹.

The main artefact of the simulated response is that the secondary chirps (positioned between the main chirps) are too pronounced. This is probably because the dispersion relation of the underlying model (see Figure 5) is too linear in the regions directly to the left and right of the point $\beta = q$.

5. CONCLUSIONS

A numerical method for deriving modal parameters from a physical model of a helical spring has been presented. A finite difference scheme with a spatial order of accuracy of 98 was employed to achieve a numerical dispersion relation that is a highly accurate up to about 15 kHz, leading to a complete set of a modal parameters that can be directly employed in an efficient and accurate modal reverb algorithm.

The methodological novelty resides mainly in the use of repeated boundary conditions to eliminate the multiple ghost-points that arise near the boundaries when using a higher-order centered scheme. The scheme is unconditionally stable under the assumption that the finite difference matrix \mathbf{D} is negative definite, which

¹<http://www.socasites.qub.ac.uk/mvanwalstijn/dafx20a/>

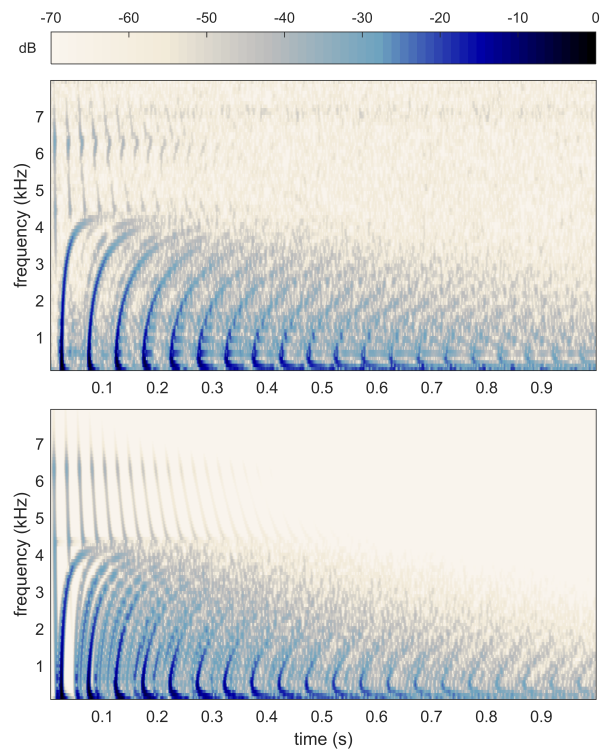


Figure 7: Impulse response spectrograms. Top: Measured response. Bottom: Simulation with modal filtering and low-frequency dispersion manipulations applied.

was verified in all cases explored within the study. A formal stability proof can probably be arrived at via energy analysis, which is the subject of ongoing research. A related investigative route is the application of existing methods for boundary treatment with higher-order in space schemes, including Summation-By-Parts (SBP) operators and Simultaneous Approximation Term (SAT) methods (see [21] for an overview). In addition, it is likely to be beneficial to frame the problem in semi-discrete from (i.e. no temporal dis-

cretisation), and/or to calculate higher-order finite difference coefficients via optimisation.

The main limitation of the diagonalisation approach taken in this paper is that the matrix eigenvalue calculation required for the similarity transformation in eq. (61) is computationally costly for the number of interior nodes minimally required for spring reverb tank modelling. This means that, while the modal reverb algorithm itself easily runs in real-time, there is little prospect of adapting the modal parameters on the fly in response to changes in the system parameters κ , q , and γ , at least not without the use of interpolated look-up table methods. While the same holds in principle for the damping parameters (ϕ and σ), the relationship between these and the modal damping factors α_j could probably quite easily be retro-modelled to facilitate on-line variation. Alternatively, modal damping could altogether be more freely defined and controlled.

In principle, the numerical methodology presented here can be directly applied to more complex and accurate descriptions of the system dynamics. A few *a priori* considerations are offered here. Firstly, finite precision effects will come into play in the eigenvalue calculation when increasing the size of the finite difference matrices significantly beyond about 3000×3000 , unless floating-point variables are specified using more bits than with double-precision. Secondly, the accuracy at the boundaries resulting with the simplified boundary conditions specified in eqs. (7,8) will not necessarily transfer to models featuring magnetic bead resonators. Finally, a holistic approach will probably involve formal testing of the perceptual significance of the resulting objective improvements.

6. REFERENCES

- [1] L. Hammond, "Electrical musical instrument," 1941, US Patent No. 2230836.
- [2] J. Parker and S. Bilbao, "Spring reverberation: a physical perspective," in *Proc. of 12th Int. Conf. on Digital Audio Effects (DAFx-09)*, 2009, pp. 416–421.
- [3] S. Bilbao and J. Parker, "Perceptual and numerical aspects of spring reverberation modeling," in *Proc. of 20th Int. Symp. on Music Acoustics*, 2010.
- [4] J. S. Abel, D. P. Berners, S. Costello, and J. O. Smith III, "Spring reverberation using dispersive allpass filters in a waveguide structure," in *Proc. of the 121st AES Convention, San Francisco*, 2006.
- [5] V. Välimäki, J. Parker, and J. S. Abel, "Parametric spring reverberation effect," *Journal of the AES*, vol. 59, no. 7–8, pp. 547–562, 2010.
- [6] A. C. Young, "Artificial reverberation unit," 1963, US Patent No. 3106610.
- [7] J. Parker, "Efficient dispersion generation structures for spring reverb emulation," *EURASIP Journal on Advances in Signal Processing*, 2011.
- [8] H. Gamper, J. Parker, and V. Välimäki, "Automated calibration of a parametric spring reverb model," in *Proc. of 14th Int. Conf. on Digital Audio Effects (DAFx-11)*, 2011, pp. 416–421.
- [9] J. S. Abel, S. Coffin, and K. Spratt, "A modal architecture for artificial reverberation with application to room acoustics modeling," in *Proc. of the 137th AES Convention*, 2014.
- [10] J. S. Abel and E. K. Canfield-Dafilou, "Dispersive delay and comb filters using a modal structure," *IEEE Signal Processing Letters*, vol. 26, no. 12, pp. 1748–1752, 2019.
- [11] S. Bilbao and J. Parker, "A virtual model of spring reverberation," *IEEE Trans. on Audio Speech and Language Processing*, vol. 18, no. 4, pp. 799–808, 2010.
- [12] S. Bilbao, "Numerical simulation of spring reverberation," in *Proc. of the 16th Int. Conf. on Digital Audio Effects (DAFx-13)*, 2013.
- [13] W. H. Wittrick, "On elastic wave propagation in helical springs," *Int. Journal of Mechanical Sciences*, vol. 8, no. 1, pp. 25–47, 1966.
- [14] V. Välimäki, J. Parker, L. Savioja, J. O. Smith, and J. S. Abel, "Fifty years of artificial reverberation," *IEEE Trans. on Audio Speech and Language Processing*, vol. 20, no. 5, pp. 1421–1448, 2011.
- [15] T. Tarnopolskaya, F. de Hoog, N. H. Fletcher, and S. Thwaites, "Asymptotic analysis of the free in-plane vibrations of beams with arbitrarily varying curvature and cross-section," *Journal of Sound and Vibration*, vol. 196, no. 5, pp. 659 – 680, 1996.
- [16] R. S. Lakes, *Viscoelastic Solids*, CRC Press, 1999.
- [17] Fornberg, "Generation of finite difference formulas on arbitrarily spaced grids," *Mathematics of Computation*, vol. 51, no. 184, pp. 699–706, 1988.
- [18] J. Parker, "private communication, February 2019.
- [19] L. R. Rabiner and B. Gold, *Theory and Application of Digital Signal Processing*, Prentice-Hall, 1975.
- [20] M. van Walstijn and S. Mehes, "An explorative string-bridge-plate model with tunable parameters," in *20th Int. Conf. on Digital Audio Effects (DAFx-17)*, 2017, pp. 291–298.
- [21] B. Gustafsson, *High Order Difference Methods for Time Dependent PDE*, Springer-Verlag Berlin Heidelberg, 2008.

Appendix: Remarks on Stability

Ignoring damping and external forces, consider the single-frequency ansatz

$$\mathbf{w}^n = e^{j\omega n \Delta_t} \mathbf{p}, \quad (75)$$

where \mathbf{p} represents the numerical modal shape vector for frequency ω . Substitution into the lossless version of (52), with the averaging operator μ_2 in place, yields

$$\underbrace{-4 \tan^2\left(\frac{1}{2}\omega \Delta_t\right)}_{\lambda} \mathbf{p} = \mathbf{D}\mathbf{p}, \quad (76)$$

from which it is clear that the term λ must be an eigenvalue of \mathbf{D} , and \mathbf{p} must be the associated eigenvector. We now consider the same for the case when the averaging operator is not employed (i.e. replacing μ_2 with 1 in eq. (52)), and obtain

$$\underbrace{-4 \sin^2\left(\frac{1}{2}\omega \Delta_t\right)}_{\lambda} \mathbf{p} = \mathbf{D}\mathbf{p}. \quad (77)$$

So for a given eigenvalue of \mathbf{D} , we can derive the associated frequency. For the two cases, this gives

$$\omega = \frac{2}{\Delta_t} \tan^{-1}\left(\frac{1}{2}\sqrt{-\lambda}\right) \quad (\text{with } \mu_2), \quad (78)$$

$$\omega = \frac{2}{\Delta_t} \sin^{-1}\left(\frac{1}{2}\sqrt{-\lambda}\right) \quad (\text{without } \mu_2). \quad (79)$$

If \mathbf{D} is a negative definite matrix (not proven here but confirmed in all numerical experiments), the eigenvalues lie in the range $\lambda_{\min} \leq \lambda < 0$. So in the case of no averaging operator, the frequency will become complex-valued with a negative real part when $\lambda < -4$; from (75) that means the solutions will then be exponentially growing in time. From (76) and (77) it can be seen that the $|\lambda_{\min}|$ increases with Δ_t . Hence without the averaging operator in place, there will be a stability condition to observe, and Δ_t will have to be chosen sufficiently small for it to be met. On the other hand if the averaging operator is employed, the frequency ω will always be real-valued, because the inverse tan function exists across the whole real number axis. Hence provided that \mathbf{D} is a negative definite matrix, the numerical system will then be stable, with no condition on the time step Δ_t .